frontiers in Nanotechnology

ORIGINAL RESEARCH
published: 10 March 2022
doi: 10.3389/fnano.2022.851041

IoT-Enabled Integrated Smart Wound Sensor for Multiplexed Monitoring of Inflammatory Biomarkers at the Wound Site

*Tanzila Noushin, Nafize Ishtiaque Hossain and Shawana Tabassum**

Biosensors and Bioinformatics Laboratory, Department of Electrical Engineering, The University of Texas at Tyler, Tyler, TX, United States

Chronic wounds that stall at the inflammatory phase of healing may create several life-threatening complications such as tissue damage, septicemia, and organ failures. In order to prevent these adverse clinical outcomes and accelerate the wound healing process, it is crucial to monitor the wound status in real-time so that immediate therapeutic interventions can be implemented. In addition, continuous monitoring of the wound status can prevent drug overdose at the wound site, leading to on-demand and personalized drug delivery. Inflammatory mediators, such as Interleukin-6 (IL-6) and Interleukin-10 (IL-10) are promising indicators for the progression of wound healing and predictors of disease severity. Toward this end, this work reports a flexible wound patch for multiplexed monitoring of IL-6 and IL-10 at the wound site in order to provide real-time feedback on the inflammation phase of the wound. An optimized composition of gold nanoparticles integrated multiwalled carbon nanotube was demonstrated to improve sensor performance substantially. The sensor also exhibited excellent repeatable, reversible, and drift characteristics. A miniaturized Internet-of-things (IoT)-enabled potentiostat was also developed and integrated with the flexible sensor to realize a wearable system. This IoT-enabled wearable device provides a smart and cost-effective solution to improving the existing wound care through continuous, real-time, and *in-situ* monitoring of multiple wound biomarkers.

Keywords: chronic wounds, electrochemical sensor, smart wound dressing, wearable sensor, multiplexed sensor, internet-of-things, IL-6, IL-10

OPEN ACCESS

Edited by:
Long Que,
Iowa State University, United States

Reviewed by:
Liang Wang,
Chongqing Institute of Green and Intelligent Technology (CAS), China
Akash Bachhuka,
University of Rovira i Virgili, Spain

****Correspondence:***
Shawana Tabassum
stabassum@uttyler.edu

Specialty section:
This article was submitted to Biomedical Nanotechnology, a section of the journal Frontiers in Nanotechnology

Received: *08 January 2022*
Accepted: *17 February 2022*
Published: *10 March 2022*

Citation:
Noushin T, Hossain NI and Tabassum S (2022) IoT-Enabled Integrated Smart Wound Sensor for Multiplexed Monitoring of Inflammatory Biomarkers at the Wound Site. Front. Nanotechnol. 4:851041. doi: 10.3389/fnano.2022.851041

1 INTRODUCTION

Wounds are ruptured skin caused by accidents or chronic conditions, including diabetes mellitus, vascular diseases, infection, cancer, or surgery (Sen et al., 2009). Wound healing is a four-step process: hemostasis, inflammation, proliferation, and maturation (Williams and Barbul, 2003; Darby et al., 2014; Han and Ceilley, 2017; Serra et al., 2017; Pourshahrestani, et al., 2020). The successful completion of these four stages is essential for wound healing, while interrupting one or more steps causes prolonged non-healing wounds, otherwise known as chronic wounds, which fail to proceed through the normal phase of recovery (Tonnesen et al., 2000; Menke et al., 2007; Gurtner et al., 2008; Mehmood et al., 2014; Farahani and Shafiee, 2021). Approximately 1.5-2 million people in Europe are suffering from chronic wounds, whereas in the US, the number has crossed 6.5 million,

presenting a significant economic burden on the healthcare system with the treatment cost reaching up to 25 billion USD per year (Zimlichman et al., 2013; Phillips et al., 2016). As obesity and diabetes increase in the elderly population, chronic wound cases are increasing more rapidly among aged people (Clayton and Elasy, 2009; Sen et al., 2009; Standl et al., 2019).

Recent research thrust on chronic wounds has identified several wound biomarkers, which can be categorized into physicochemical parameters, enzymes, metabolites, and bacterial pathogens (Brown et al., 2018; O'Callaghan et al., 2020; Mota et al., 2021). Wound temperature, moisture, pH, and oxygenation are classified as physicochemical parameters, while uric acid and lactic acid are identified as metabolites. In addition, the presence of different bacteria, including *P. aeruginosa*, *E. coli*, and *B. fragilis* at the wound sites, results in an accumulation of pyocyanin, which is the primary bacterial metabolite (McLister et al., 2017; Mota et al., 2021). However, to date, studying the real-time immune regulation of skin wound healing is heavily unexplored. The immune cells secrete a cascade of signaling molecules (known as inflammatory mediators) including pro-inflammatory cytokines such as tumor necrosis factor-α (TNF- α), Interleukin-1β (IL-1β), Interleukin-6 (IL-6), and Interleukin-12 (IL-12), and anti-inflammatory cytokines such as Interleukin-10 (IL-10), Interleukin-4 (IL-4), and Interleukin-13 (IL-13) (Pẽña and O'Neill, 2014). The primary function of anti-inflammatory cytokines is to mediate/suppress the inflammation. A delicate balance between the pro-and anti-inflammatory responses is crucial to the orderly and timely healing of wounds (Kolaczkowska and Kubes, 2013; Mantovani et al., 2013; Novak and Koh, 2013; Wilgus et al., 2013; McLister et al., 2014; Oliveira et al., 2016; McLister et al., 2017; Kundu, et al., 2020). Therefore, it is noteworthy that real-time detection and monitoring of both pro-and anti-inflammatory elements of the immune system is essential for the effective management of chronic wounds.

Conventional treatment for chronic wounds involves drug-loaded wound dressings tailored to the wound status (Brown et al., 2018). However, these dressings fail to provide real-time feedback on the progression and healing of wounds, thereby delaying the treatment and subsequent recovery. Traditional wound monitoring relies on physical inspection and microbiological assessment (Bandodkar et al., 2016; Li et al., 2021). Physical examination involves successive bandage removal that suffers from a lack of accuracy. Although the microbial assays provide a more conclusive result, they are time-consuming, invasive, and ineffective, particularly for detecting bacterial pathogens that invade deeper tissues (Brown et al., 2018). In contrast, wearable wound patches can provide accurate, non-invasive, real-time, and continuous monitoring of the dynamics of chronic wounds. Existing smart wound dressings employ colorimetric methods to detect pH (Kassal et al., 2017; Pan et al., 2019), fluorometric methods to detect bacteria (Zhou et al., 2018), O_2 (Ochoa et al., 2020), and H_2O_2 (Wu et al., 2020), and electrochemical techniques to monitor lactate and oxygen (Ashley et al., 2019). Clinical translation of these wearable devices requires careful consideration of several aspects, including biocompatibility, flexibility, and connectivity (Bandodkar et al., 2016; Li et al., 2021). However, these sensors do not provide a real-time indication of the immune system response and progression at the wound site. Therefore, smart wound dressings that can non-invasively monitor the elements of the immune system at the wound site and send feedback to physicians in real-time are crucial to get a fundamental understanding of the interplay among different molecules and develop an effective wound management protocol.

This work reports a smart wound patch comprising a multiplexed electrochemical transduction unit and an integrated data processing and transmission framework. **Figure 1** shows the overview of the entire system. The electrochemical sensor was screen-printed on a flexible polyethylene terephthalate (PET) sheet attached to a sterile wound dressing. The electrode surface faced down, toward the wound site (**Figure 1A**). The sensor features multiplexed monitoring of IL-6 and IL-10 on a single chip. Gold nanoparticles integrated multiwalled carbon nanotube (AuNP-MWCNT) bundles were synthesized and optimized to improve the sensitivity, limit of detection, and stability of the electrochemical measurements (Silva et al., 2018). The versatile properties of MWCNT including ultra large active surface area, fast electron mobility, high strength, and chemical inertness, make them ideal for developing new generation of highly sensitive and stable sensors to detect ultralow levels of analytes in body fluids (Oliveira and Morais, 2018). The MWCNT nanocomposite created a three-dimensional matrix on the electrode surface, thereby enhancing the loading of immobilized layers and antibody molecules. Incorporation of AuNPs introduced additional attachment sites in the MWCNT matrix. The complete system also included a custom-made data processing and internet-of-things (IoT)-based wireless transmission unit (**Figures 1B,C**). Optical images of the complete wearable system are shown in **Supplementary Figure S1**. The incorporation of IoT-based monitoring enables the real-time tracking of IL-6 and IL-10 levels at the wound site. The sensor was also tested for mechanical deformations to justify its practical use. Overall, the integrated system demonstrates the potential for real-time and continuous measurements of inflammatory mediators at the wound site.

2 MATERIALS AND METHODS

2.1 Reagents

Simulated wound fluid exudate (BZ292) was obtained from Bio Chemazone (Alberta T6B 3P3 Canada) while the other reagents such as Prussian blue (PB), potassium hexacyanoferrate (III) {$K_3[Fe(CN)_6]$}, potassium chloride (KCl), hydrochloric acid (HCl), iron (III) chloride ($FeCl_3$, thiol cross-linker acid solution, N′-ethylcarbodiimide hydrochloride (EDC), N-Hydroxysuccinimide (NHS), bovine serum albumin (BSA), graphene ink, silver/silver chloride (Ag/AgCl) paste, hydrogen tetrachloroaurate (III) hydrate ($HAuCl_4$), and trisodium citrate were purchased from Sigma Aldrich (St. Louis, MO). The multi-walled carbon nanotube (MWCNT) was obtained from ACS Material (Pasadena, CA). The Interleukin-6 and Interlukin-10 protein

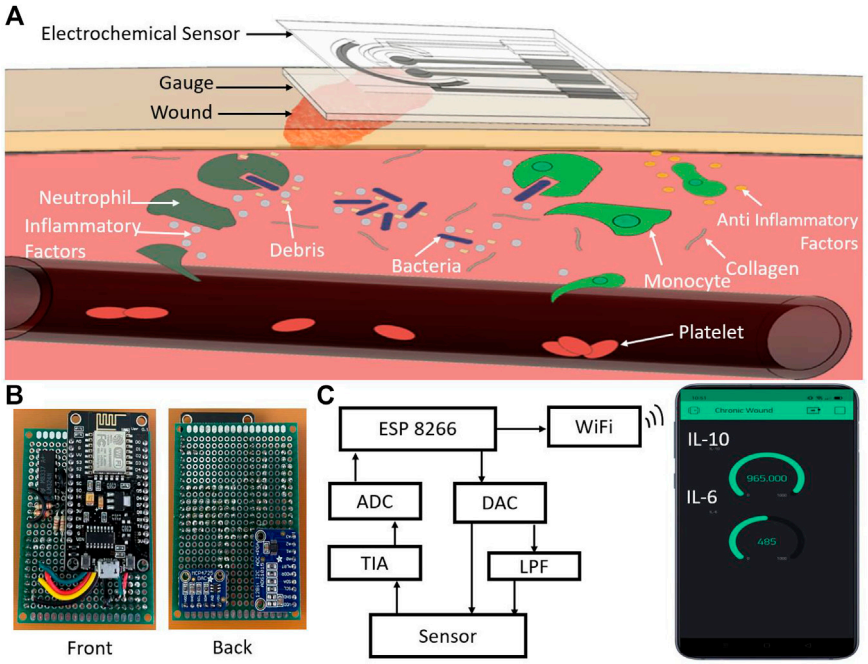

FIGURE 1 | (A) Schematic illustration of the flexible smart wound dressing placed at the wound site for multiplexed monitoring of IL-6 and IL-10. **(B)** Optical image of the front and back side of the developed IoT-enabled potentiostat. **(C)** Block diagram of the IoT-enabled chronic wound analysis system. ADC: Analog-to-digital converter, DAC: Digital-to-analog converter, LPF: Low-pass filter, and TIA: Transimpedance amplifier.

and antibody were purchased from R&D Systems (Minneapolis, MN). IL-6 and IL-10 proteins were spiked in simulated wound fluid (SWF) at varying concentrations ranging from 0.1 pg/ml to 1,000 pg/ml.

2.2 Instrumentation

Cyclic voltammetry (CV) and chronoamperometry analyses were performed through CHI 660E electrochemical workstation (CH Instruments, Inc.). The following parameters were used for CV: range, −0.2–+2.0 V; scan rate, 50 mV/s; incremental potential, 0.01 V. The following parameters were used for CA: pulse amplitude, 0.5 V; time interval, 0.1 s, and run time, 20 s. It is to be noted that, similar CV results were obtained with our custom-made potentiostat (**Figure 1B**), as explained under the Results and Discussion section. A PrismCut Vinyl Cutter (USCutter) was used for cutting and screen printing the electrodes. For characterizing mechanical deformations of the sensor, a compact, motorized translation stage (Thorlabs) was used. The motorized base was programmed to bend the sensor from 0° to 90° angle and return to the initial 0° position. This entire cycle of bending was conducted 100 times.

Zeiss Supra 55VP scanning electron microscope (SEM) and Nicolet Avatar 360 E.S.P. ATR-FTIR spectrometer were utilized to characterize the AuNP decorated MWCNT coatings.

2.3 Design of the Multiplexed Electrodes

The electrochemical sensor design contained four layers: 1) Screen-printed electrodes (SPEs) having two working electrodes (WEs) for detecting two cytokines, one counter electrode (CE), and one reference electrode (RE), 2) a hydrophobic polyethylene terephthalate (PET) sheet patterned with the SPEs, 3) a medical-grade sterile wound dressing as the underlying substrate, and 4) a second medical-grade porous gauge for protecting the electrode surface.

A low-cost and roll-to-roll technique was used to manufacture the sensors on a large scale (**Figure 2A**) (Pereira et al., 2021). **Figure 2B** demonstrates the stepwise fabrication of the SPEs. The electrode patterns were designed in AutoCAD Fusion 360 software and then imported to a benchtop craft cutter for cutting the electrode patterns on an 85 μm thick polyvinyl chloride (PVC) sheet (HTVRont). The PVC sheet was covered with a transfer tape that worked as the masking layer. Firstly, the taped PVC sheet was loaded into the craft cutter, and the SPE patterns were cut through the sheet (**Figures 2Bi–iii**). The optimized parameters for the cutter blade were force 4.5 N and speed 30 mm/s. The blade was run twice over the PVC sheet to generate a precise pattern. Next, the transfer tape was peeled off from the WEs and the CE areas, and graphene ink was uniformly screen-printed to the exposed regions with a squeegee (**Figure 2Biv**). Likewise, the exposed regions of RE were screen printed with Ag/AgCl paste (**Figure 2Biv**). The electrodes were cured at 100°C temperature for 60 min in a convection oven. Afterward, the SPE pieces were removed from the base and transferred to a pre-cut 125 μm thick PET sheet (Grainger) (**Figures 2Bv, vi**). Finally, the PET sheet was placed on a sterile cotton dressing. A second medical-grade porous gauge was attached on the electrode surface such that wound exudates can get absorbed by the gauge and flow to the electrode surface, while simultaneously protecting the delicate wound

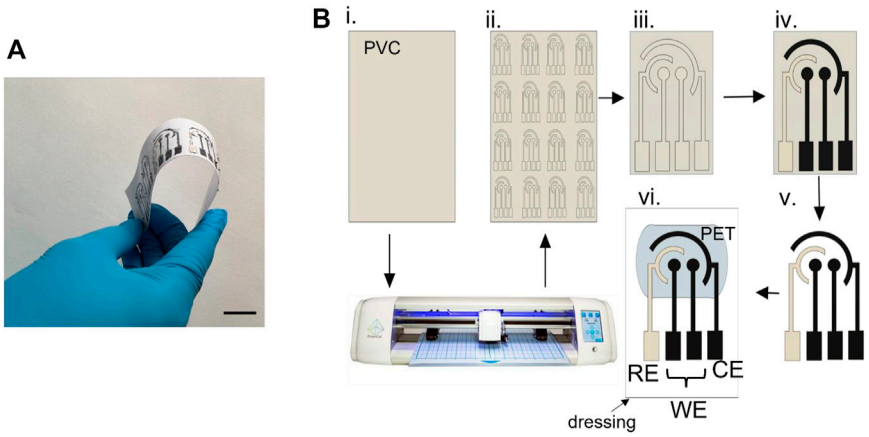

FIGURE 2 | (A) Roll-to-roll production of the flexible multiplexed sensor array. Scale bar, 2 cm. **(B)** Stepwise fabrication process of the screen-printed electrodes.

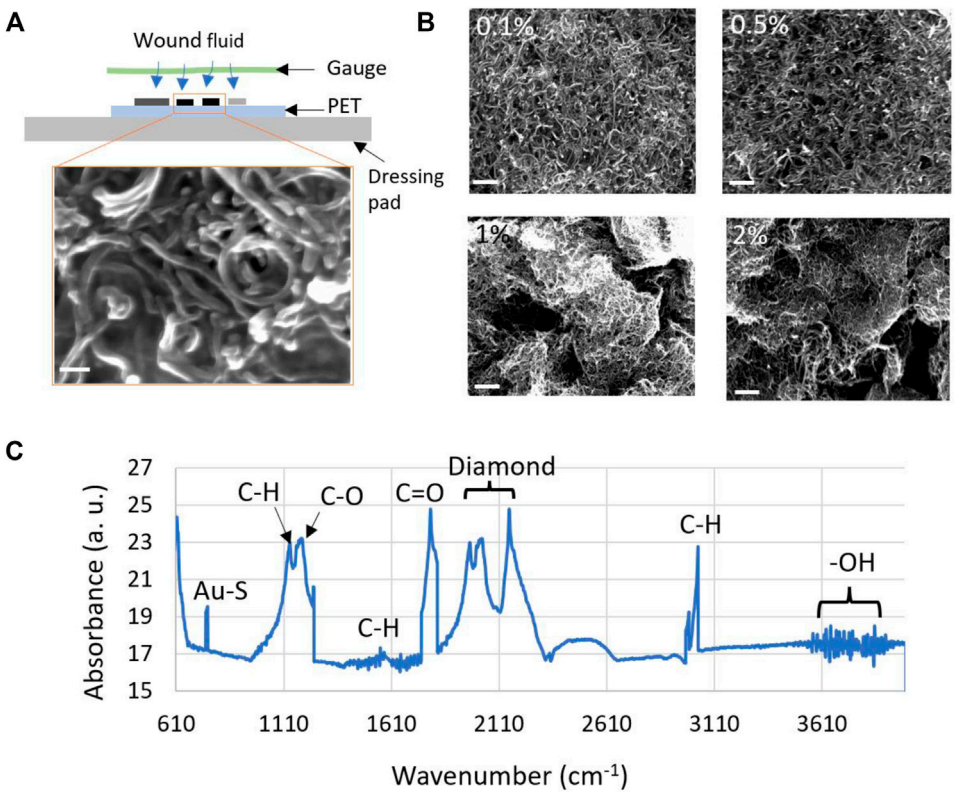

FIGURE 3 | (A) Cross-sectional view of the electrochemical sensor fabricated on a wound dressing pad. The wound fluid diffuses to the sensor surface through a porous gauge. Inset of **(A)** shows the SEM images of the 0.5% (w/v) AuNP decorated MWCNT coating on the two working electrodes. The scale bar corresponds to 100 nm. **(B)** SEM images showing the morphology of four (0.1, 0.5, 1.0 and 2.0%) different dispersions of AuNP decorated MWCNT coating. All the scale bars represent 1 μm. **(C)** Characterization of the AuNP-MWCNT coating using FTIR.

area from foreign body response (due to the sensor electrodes). The cross-section of the sensor is shown in **Figure 3A**. The overall dimension of the sensing area was 2 cm × 1.4 cm. The screen-printing method with a benchtop craft cutter enables low-cost and rapid bulk manufacturing of the electrodes.

2.4 Preparation of AuNP-MWCNT Coating

To selectively detect IL-6 and IL-10, the WEs were immobilized with a number of chemical layers. This work features gold nanoparticles decorated multiwalled carbon nanotube (AuNP-MWCNT) composite coating as the protein-sensitive layer.

Preparation of the AuNP-MWCNT dispersion started with the formation of AuNPs using the Turkevich method (Turkevich et al., 1951; Shakila and Pandian, 2006). Briefly, 30 ml of 0.01% (w/v) tetra chloroauric (III) acid ($HAuCl_4$) was set to boil on a hotplate with constant stirring. After the boiling started, 1 ml of 1% sodium citrate was added slowly. The solution was stirred for 15 min to complete the reaction. The obtained dispersion was centrifuged at 14,000 rpm for 20 min to remove the unreacted $HAuCl_4$ and sodium citrate. The resulting precipitate was collected, which was redispersed in 200 ml of Milli-Q water. The above procedure resulted in mean AuNPs of 25 nm (Turkevich et al.,1951), which was also confirmed through scanning electron microscope images (**Figure 3**). We selected this specific size of AuNPs because it provided highest current response, as described in the **Supplementary Table S1** and **Supplementary Figure S2**.

Synthesis of -OH functionalized MWCNT was carried out by treating the MWCNT with 3M nitric acid solution under constant stirring for 24 h. The functionalized MWCNT was washed thoroughly with Milli-Q water and subsequently dried at 80°C for 12 h in a convection oven (Ghica and Brett, 2013; Silva et al., 2018).

The AuNP-MWCNT composite coating was synthesized by dispersing equal volumes of AuNP and MWCNT stock solutions in 1% (w/v) chitosan dissolved in 1% (v/v) acetic acid solution and sonicating for 8 h. Four different AuNP-MWCNT dispersions (0.1, 0.5, 1 and 2% (w/v)) were prepared by following this procedure.

2.5 Chemical Functionalization of Working Electrodes

The WEs were first electrodeposited with Prussian Blue (PB) (worked as a redox mediator) and AuNP-MWCNT by running 200 voltammetric cycles for potential ranging from −0.3 to +1.2 V at a scan rate of 50 mV/s in a plating solution containing 2.5 mM K_3 [Fe $(CN)_6$], 2.5 mM $FeCl_3$, 0.1 M KCl, 0.1 M HCl and 1 mg ml^{-1} AuNP-MWCNT. Four different dispersions of AuNP-MWCNT, 0.1, 0.5, 1 and 2% (w/v), were used to do electrodeposition on four electrodes (Shakila and Pandian, 2006; Noushin and Tabassum, 2022).

Secondly, the AuNP-MWCNT-PB immobilized WEs were coated with a thiol cross-linker [HS $(CH_2)_4$–COOH]. The thiol functional groups of the linker formed Au-S bonds with the AuNPs, while the carboxyl groups facilitated covalent binding to EDC molecules of the next layer to form an intermediate O-acylisourea. A 1 mM of thiolated linker solution was prepared in PBS (pH = 7) and 4 µL of this solution was drop cast on the WEs.

Thirdly, the WEs were functionalized with anti-IL6/anti-IL10 molecules via EDC-NHS coupling chemistry (Ali et al., 2018). In this regard, 0.2M EDC and 0.05M NHS solutions were mixed with a 1 mg/ml antibody solution at a 1:1 volume ratio. The NHS molecules reacted with primary amines of antibody to form amine-reactive stable NHS ester. A 4 µL of antibody solution was drop cast on the WEs that were stored inside a humid chamber at 4°C for 12 h. This step allows the conjugation of antibodies to the WE surface.

Finally, 2 mg/ml solution of bovine serum albumin (BSA) was drop-cast on the WEs to block the non-specific binding sites.

3 RESULTS AND DISCUSSION

3.1 Characterization of the Chemically Functionalized Electrode

The AuNP-MWCNT coated and uncoated electrodes were characterized by scanning electron microscopy (SEM), Fourier transform infrared (FTIR) spectroscopy, cyclic voltammetry (CV), and chronoamperometry (CA).

3.1.1 Scanning Electron Microscopy

The size, distribution, and morphology of AuNP decorated MWCNT network was visualized by scanning electron microscopy (SEM). **Figure 3A** shows the cross-section of the fabricated sensor and the SEM image of the formation of AuNP-MWCNT coating on the working electrodes. **Figure 3B** illustrates a comparative analysis of the four AuNP-MWCNT coatings, which support our selection of 0.5% (w/v) coating for protein tests (as is explained later under Results and Discussion and shown in **Figure 5**). The coatings prepared from 0.1 to 0.5% (w/v) dispersions exhibited homogeneous and uniform surface morphology, whereas the denser dispersions (i.e., 1.0 and 2.0%) resulted in non-homogeneous, uncontrolled, and multiple-layered coatings. As a result, a significant number of the AuNPs were buried inside the MWCNT layers, which reduced the electrochemical conductivity of the nanocomposite. Therefore, as is also explained under Results and Discussion, the denser MWCNT layers resulted in poor sensor performance (see **Figure 5**). The average size of the AuNPs was found to be 25.2 ± 4.7 nm.

3.1.2 Fourier Transform Infra-Red Spectroscopy

The AuNPs decorated MWCNT nanocomposite was characterized with an Attenuated Total Reflectance (ATR)-FTIR spectrometer. Absorption spectra were recorded at a rate of 16 scans per sample in the 500–4,000 cm^{-1} wavenumbers range (**Figure 3C**). Omnic software was used to analyze the recorded spectra. The absorption peaks between 3,500 and 4,000 cm^{-1} confirm the presence of the -OH functional groups, while the peaks in the 2,975–3,065 cm^{-1}, 1,390–1700 cm^{-1}, and 1,100–1,160 cm^{-1} range represent the C-H bonds. The presence of C-O and C = Ö bonds are confirmed by the peaks at 1,200 and 1790 cm^{-1}, respectively. The single peak at ~750 cm^{-1} corresponds to Au-S bonds from gold nanoparticles. The additional peaks in the 1950–2,210 cm^{-1} range represent the artifacts of the diamond ATR setup (Fang et al., 2018). The FTIR results are in good agreement with previous reports (Thamri et al., 2016), confirming the presence of gold decorated -COOH functionalized MWCNTs in the coating.

3.1.3 Electrochemical Characterization

Unless otherwise stated, all sensor characterizations were performed in SWF (pH = 7.4). Cyclic voltammetry (CV)

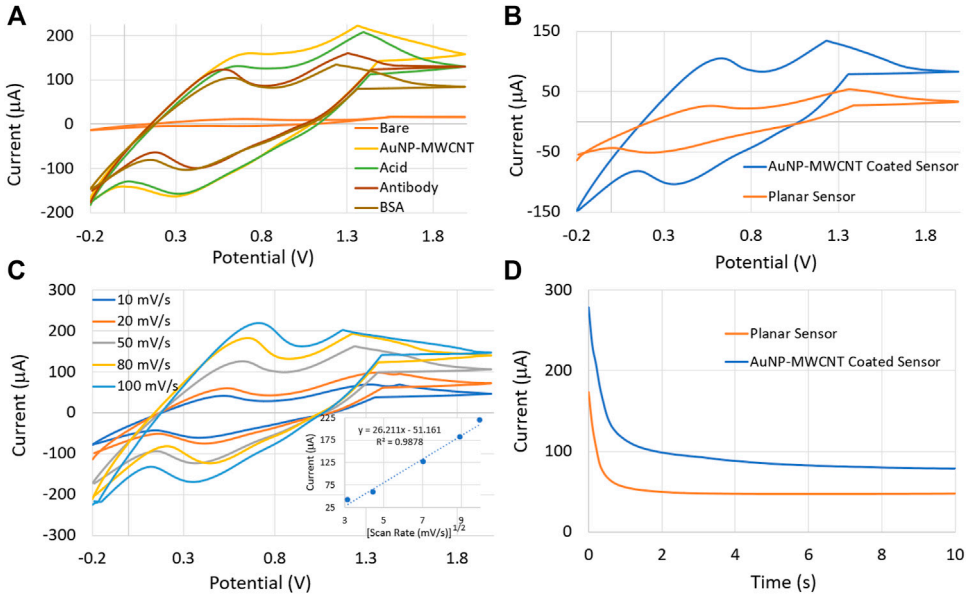

FIGURE 4 | (A) Cyclic Voltammetry (CV) plots for sequentially deposited coatings on the sensor surface. **(B)** CV characteristics of the AuNP-MWCNT coated and planar sensors. **(C)** CV characteristics as a function of scan rate. The inset demonstrates the diffusion-limited behavior of the sensor. **(D)** Chronoamperometry (CA) characteristics of the planar and AuNP-MWCNT coated sensors.

technique was used to investigate the redox performance of the sensor for different immobilized coatings. **Figure 4A** demonstrates the CV plots for bare graphene WE and after sequentially adding AuNP-MWCNT, linker acid, antibody, and BSA on the electrode surface. The voltammograms were performed in the potential range of −0.2–+2.0 V, with a scan rate of 50 mV/s. The addition of different layers reduced the redox current due to the insulating property of the immobilized layers that slowed down electron transfer (Silva et al., 2018). The oxidation and reduction peaks occurred at 0.55 and 0.4 V, respectively. **Figure 4B** illustrates the CV scans for one AuNP-MWCNT-coated and one uncoated sensor. It is evident from the CV plots that the AuNP-MWCNT-coated sensor exhibited a ~5-fold increase in redox current than the sensor without any AuNP-MWCNT coating (also called planar/uncoated sensor). AuNP-MWCNT enhanced the electrostatic interactions owing to the abundance of electroactive surface area and attachment sites (Luo et al., 2001; Elgrishi et al., 2018) Next, the CV technique was conducted for different scan rates to analyze electron transfer kinetics through the composite coating (**Figure 4C**). As the scan rate increased from 10 to 100 mV s^{-1}, the oxidation current increased while the reduction current decreased. The peak current increased linearly with $\sqrt{scan\,rate}$ (shown at the inset of **Figure 4C**), representing a diffusion-controlled and reversible process (Ali et al., 2018). Our experimental analysis is corroborated by the Randles-Sevcik equation, which describes the effect of scan rate on the peak current in a diffusion-limited process:

$$i_p = 0.446\, n\, F\, A\, Co\left(\frac{n\, F\, v\, Do}{R\, T}\right)^{\frac{1}{2}} \quad (1)$$

Where n, A, Do, and co are the number of the transferred electrons, electrode area, diffusion coefficient, and analyte concentration, respectively. i_p represents the peak oxidation current, and v is the scan rate (Bard and Faulkner, 1980; Ali et al., 2020).

In addition, the chronoamperometry (CA) technique was employed to investigate further the sensor's redox reactivity with and without the AuNP-MWCNT coating. The CA was carried out by applying a fixed potential of 0.5 V between the working and reference electrodes. The CA results in **Figure 4D** verified that the AuNP-MWCNT-coated sensor exhibited a higher redox current, as was also measured from the CV tests illustrated in **Figure 4B**. The sensor with gold decorated MWCNT showed a response time of 6 s, while the planar sensor's response time was found to be 2 s. This minimal time lag may be attributed to the additional diffusion kinetics of the charge carriers through the AuNP-MWCNT nanocomposite matrix.

3.2 Electrochemical Behavior of IL-6 and IL-10 Sensors Under Different Electrode and Wound Parameters

The effects of different parameters including changes in the coating composition, wound pH, and bending motions, on the electrochemical behaviour of the sensors are explained in this section.

3.2.1 Influence of Different AuNP-MWCNT Dispersions

The central layer of our sensor is the AuNP-MWCNT nanocomposite coating. Therefore, we investigated the

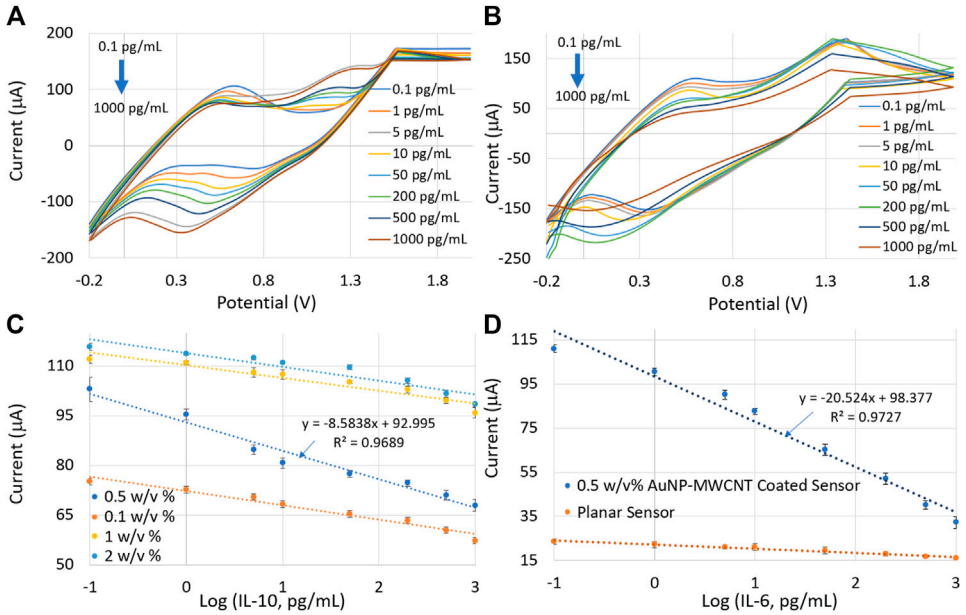

FIGURE 5 | CV plots from the 0.5% (w/v) AuNP-MWCNT-coated sensor for eight different concentrations of **(A)** IL-10 and **(B)** IL-6. **(C)** Calibration curves by plotting current versus protein concentrations for four different AuNP-MWCNT coatings. **(D)** Calibration plots showing the performance comparison of planar and AuNP-MWCNT-coated IL-6 sensors. Error bars represent three repeated measurements for each protein concentration.

influence of different AuNP-MWCNT dispersions on the performance metrics of the sensor, i.e., sensitivity and limit of detection. Four different dispersions of AuNP-MWCNT, 0.1, 0.5, 1 and 2% (w/v) were drop-cast on four identical IL-10 sensors (where we only varied the concentration of MWCNT and used the same 25 nm of AuNPs). For the electrochemical measurements of IL-6 and IL-10, eight different concentrations (ranging from 0.1 pg/ml to 1,000 pg/ml) of each protein biomarker were prepared in Simulated Wound Fluid (pH = 7.4). **Figures 5A, B** depicts the CV responses of the 0.5% (w/v) AuNP-MWCNT coated sensor spiked with varying concentrations of IL-10 and IL-6, respectively. With increasing protein concentrations, the redox current decreased due to the formation of a thicker immunocomplex layer via the binding of increased number of protein molecules with the antibodies on the sensor surface. The sensor presented a linear range of response from 0.1 pg/ml to 1,000 pg/ml protein concentrations.

It is evident from the calibration plots in **Figure 5C** that the sensor coated with 0.5% (w/v) of AuNP-MWCNT exhibited the highest sensitivity (implying the calibration plot with the largest slope) and lowest detection limit. The limit of detection (LoD) was calculated using the following equations (Ali et al., 2020), where "c" is the intercept of the calibration curve of the sensor:

$$LoB = Mean\ of\ signal\ (blank\ sample) + 1.645 \times (Std\ dev\ of\ blank\ sample) \quad (2)$$

$$Limit\text{-}of\text{-}detection\ of\ the\ signal\ (YLoD) = LoB + 1.645 \times (Std\ dev\ of\ target\ at\ low\ concentration) \quad (3)$$

$$LoD = (YLoD - c)/slope\ of\ the\ sensor\ calibration \quad (4)$$

TABLE 1 | Performance comparison of the IL-10 sensor for different AuNP-MWCNT dispersions.

AuNP-MWCNT	Sensitivity (μA (pg/mL)$^{-1}$ cm^{-2})	LoD (pg/ml)
0.1 w/v%	138.709	0.04
0.5 w/v%	273.23	7.76×10^{-3}
1 w/v %	122.195	0.5
2 w/v %	132.442	1.5

Table 1 shows the performance comparison of the sensor for four different AuNP-MWCNT dispersions. The 0.5% (w/v) AuNP-MWCNT resulted in the highest sensitivity of 273.23 μA (pg/mL)$^{-1}$ cm^{-2} and the lowest LoD of 7.76×10^{-3} pg/ml. In light of these results, 0.5% (w/v) AuNP-MWCNT was selected as the optimized coating for all the subsequent protein tests. **Table 2** shows the performance comparison of the IL-6 sensor with and without the 0.5 w/v % AuNP-MWCNT coating.

Moreover, **Figure 5D** shows the comparative analysis of the calibration plots for the 0.5% (w/v) AuNP-MWCNT coated and uncoated IL-6 sensors. The results verified a steeper calibration curve with the AuNP-MWCNT-coated sensor compared to the uncoated sensor. The sensitivities and LoDs of the IL-6 sensors with and without the AuNP-MWCNT coating are tabulated below:

3.2.2 Influence of Varying pH

Depending on the severity (healthy versus acute versus chronic wounds), wound pH can range from 4 to 8.9, wherein acidic values (pH = 4–6) imply healthy wounds

TABLE 2 | Performance comparison of the IL-6 sensor with and without the AuNP-MWCNT coating.

	Sensitivity (μA (pg/mL)$^{-1}$ cm^{-2})	LoD (pg/ml)
uncoated sensor	60.786	0.06
0.5 w/v% AuNP-MWCNT-coated sensor	653.279	9×10^{-3}

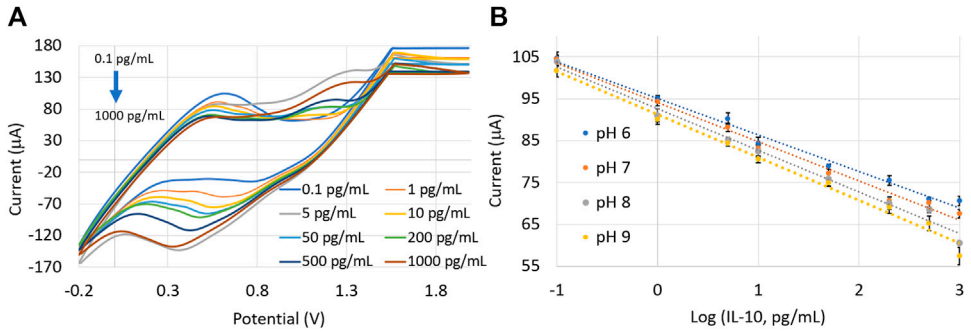

FIGURE 6 | (A) CV plots from the 0.5% (w/v) AuNP-MWCNT-coated IL-10 sensor in a pH = 7 solution. **(B)** Calibration plots in SWF solutions with varying pH (=6, 7, 8, and 9). Error bars represent three repeated measurements for each protein concentration.

and alkaline values (pH > 7) represent chronic wounds (Momoh et al., 2015; Bazbouz and Tronci, 2019). To simulate the effect of varying wound pH on the sensor performance, protein concentrations in SWF with different pH values (pH = 6, 7, 8, and 9) were prepared by adding the required amount of 0.01M HCl or 0.001M NaOH. A reduction in the oxidation peak current with increasing pH was observed (as shown in **Supplementary Figure S3** and **Figure 6**). This behavior was due to the presence of negative charges on the WE surface, originating from the citrate capped AuNPs and the carboxyl groups in the MWCNT (Zi et al., 2012). With the increase of pH, the supply of positive charges to the protein molecules declined, resulting in a decrease in the effective electrostatic interactions between the protein and the AuNP-MWCNT-modified electrode (Ardakani et al., 2009). Hence, a decline in the peak oxidation current was observed with an increase in the solution pH.

Thus, there is a direct relation of the amperometric signal with the pH: peak current increased while the slope of the calibration plot decreased with a more acidic solution (i.e., decreasing pH). Nevertheless, the sensor demonstrated satisfactory performance under different pH conditions. The calibration plots with a slope of −8.5838 ± 4.41 μA (pg/mL)$^{-1}$ and intercept of 92.995 ± 2.14 μA were measured within a linear pH range (from pH = 6–9). Taking pH = 6.5 as the reference (which is the pH of healthy wounds), the correction factors for slope and intercept (i.e., f_{slope} and $f_{intercept}$) under different pH environments can be calculated using the following equations (Wiorek et al., 2020).

$$f_{slope} = \frac{Slope(pH)}{Slope(6.5)}$$
$$f_{intercept} = \frac{intercept(pH)}{intercept(6.5)} \quad (5)$$

3.2.3 Effect of Bending

The sensor's performance was evaluated under different bending deformations to simulate the mechanical motions of human body. The sensor was placed in a motorized translation base, which was moved back and forth at a speed of 4 mm/s (**Figures 7A,B**). The sensor was bent at a maximum angle of 90°. After every bending cycle, the sensor response returned to its relaxed state in 5 s. The calibration plots of the IL-10 sensor after 50 and 100 cycles of bending are shown in **Figure 7C**. The sensor response underwent minimal variations due to the PET substrate's flexible nature coupled with the unique flexibility and porosity of the underlying textile-based wound dressing. The coefficient of variance in the intercept and slope values for the calibration plots was <8%, indicating the negligible sensor response variability to bending.

The mechanical flexibility of the sensor was further investigated with the finite-element method (FEM) based software COMSOL Multiphysics. The Solid Mechanics module was used to perform time-dependent simulation under different bending conditions. The geometry was imported from AutoCAD Fusion 360 software, and boundary conditions were applied by fixing geometry at the two opposite edges. A sinusoidal bending force was applied to evaluate the stress and displacement characteristics of the sensor. The distribution of stress along the sensor surface is shown in **Figure 7D**. The highest stress was encountered by the middle of the sensor due to the highest bending force applied in that region. Additionally, the displacement of the sensor with respect to the relaxed state is shown in **Figure 7E**.

3.3 Performance Evaluation of the Custom-Made IoT-Enabled Potentiostat

We developed an IoT-enabled potentiostat capable of measuring cyclic voltammetry responses with a predefined potential sweeping from −0.2 to 2.0 V and a scan rate of 50 mV/s. The detailed block

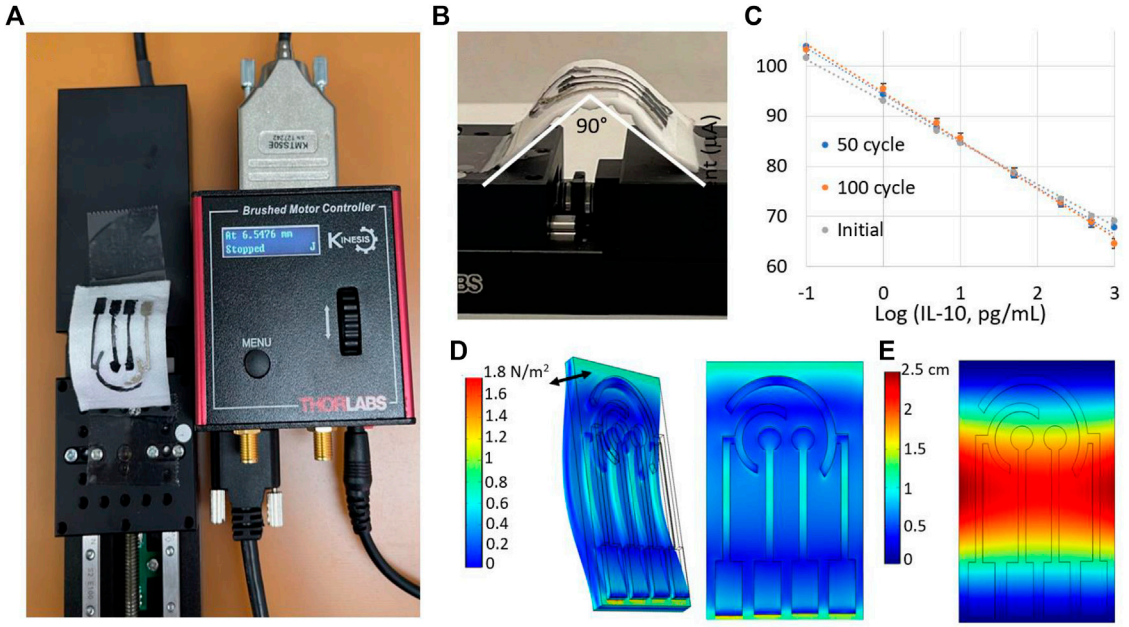

FIGURE 7 | (A) Setup for the motorized translation stage. **(B)** Evaluation of the sensor's performance under different degrees of bending, with 90° being the maximum bending angle. **(C)** Calibration plots of the IL-10 sensor after 50 and 100 cycles of bending. Measurements were repeated three times for each protein concentration. Modeling **(D)** stress and **(E)** displacement of the electrodes under sinusoidal bending. The double arrow in **(D)** shows the direction of bending.

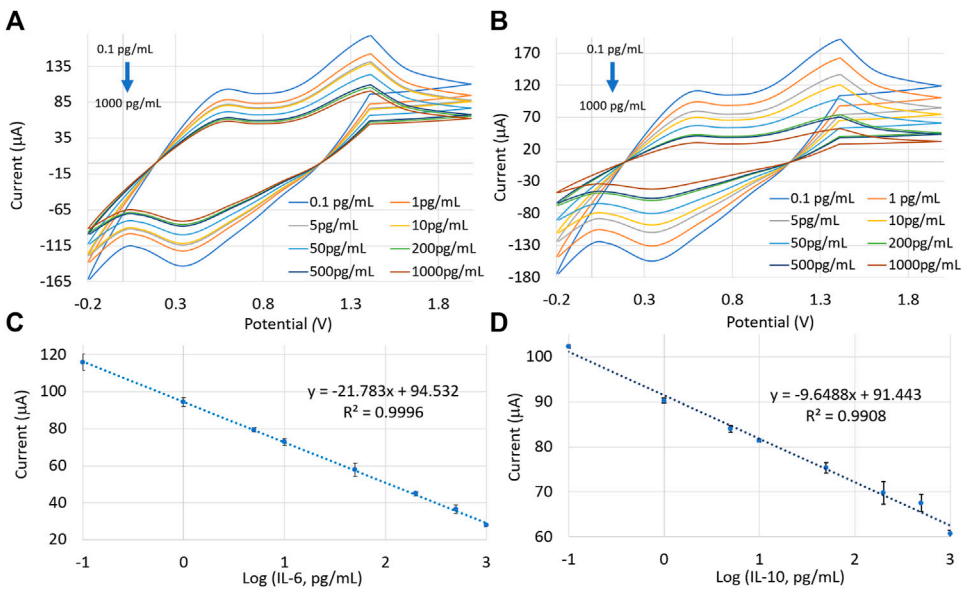

FIGURE 8 | CV plots for different concentrations of **(A)** IL-6 and **(B)** IL-10, using the developed potentiostat. Calibration curves were generated by plotting current responses as a function of **(C)** IL-6 and **(D)** IL-10 concentrations. Measurements were repeated three times for each protein concentration.

diagram is shown in **Figure 1C** and explained in **Supplementary Figure S4**. The entire electronics was enclosed in a 3D printed box that was wearable on the arm (**Supplementary Figure S1**). The wearable potentiostat was used to measure the CV responses of the sensor for eight different concentrations of IL-10 and IL-6. The Blynk IoT interface was used to transmit the data wirelessly to a smartphone application (**Figure 1C**). **Figures 8A,B** show the cyclic voltammograms in response to IL-6 and IL-10 concentrations, respectively, while the resulting calibration curves are shown in **Figures 8C,D**. The CV calibration curves obtained by the custom-developed potentiostat were nearly the same as the calibration plots generated by the commercial CHI 660E potentiostat. Error bars

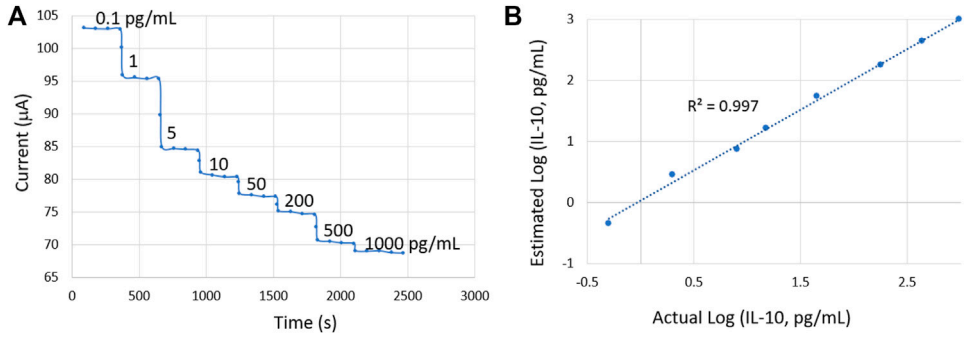

FIGURE 9 | (A) Dynamic sensor response for increasing IL-10 concentrations. **(B)** Validation of the sensor in accurately estimating unknown IL-10 concentrations.

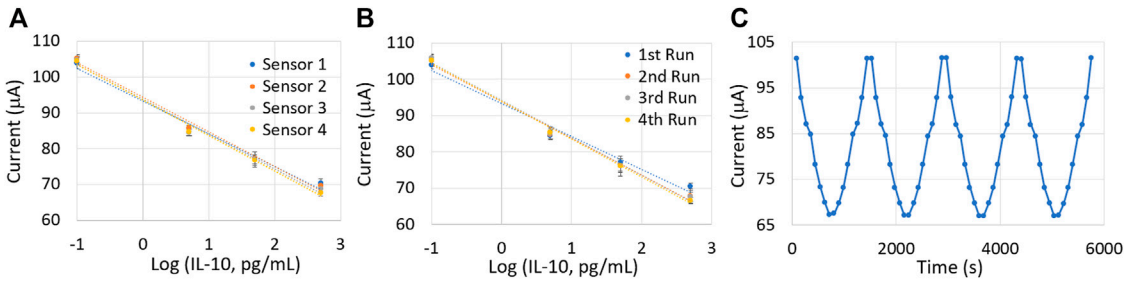

FIGURE 10 | (A) Sensor reproducibility test using four identical sensors. **(B)** Repeatability test conducted with the same sensor. **(C)** Reversibility test with cyclic variations in IL-10 concentrations. Measurements were repeated three times for each protein concentration.

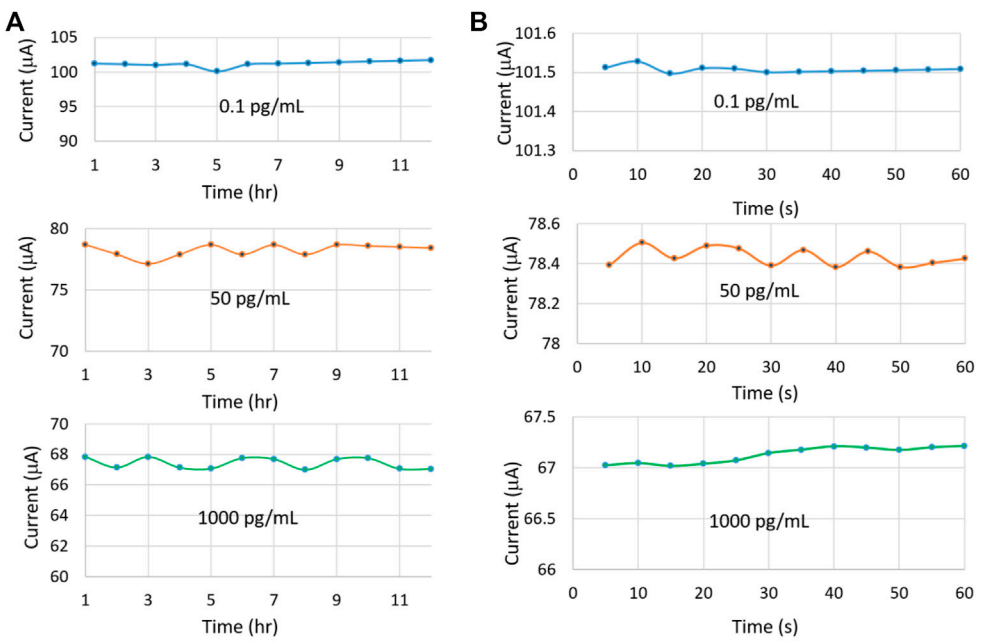

FIGURE 11 | Drift characteristics of the sensor for three different IL-10 concentrations over **(A)** 12 h and **(B)** 1 h.

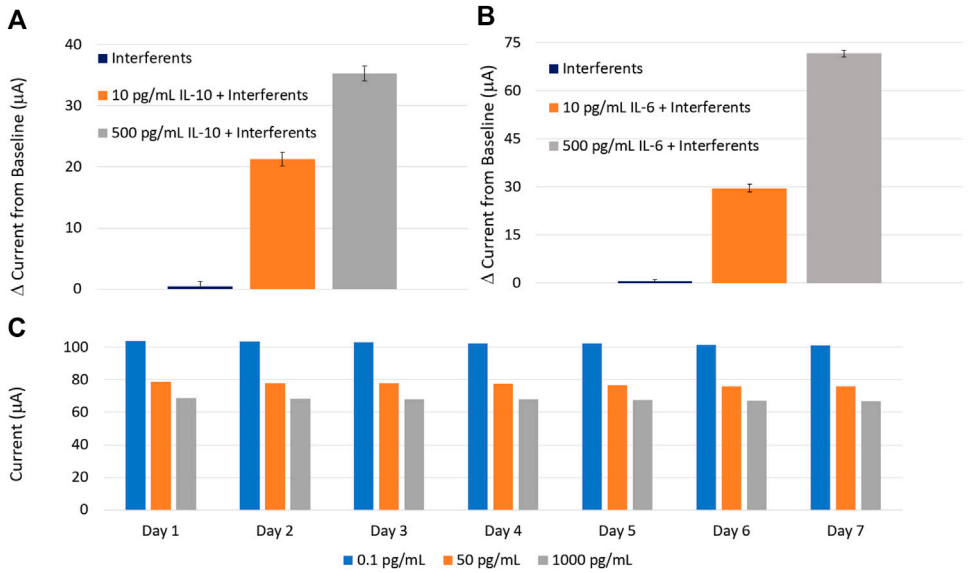

FIGURE 12 | Selectivity tests of the **(A)** IL-10 and **(B)** IL-6 sensors against common interfering species found at the wound site. **(C)** The long-term stability of the sensor over 7 days. Each measurement was repeated three times.

TABLE 3 | Comparative analysis of the developed sensor and the previous works.

Working electrode	Sensitive coating	Detection range (pg/ml)	LoD (pg/ml)	References
SPGE	AuNPs	1–15 × 10^6	0.33	Tertis et al. (2017)
GCE	p-ABA, p-ATP and AuNPs	5–1 × 10^5	1.6	Tertis et al. (2019a)
ITO	PPyr-NHS	0.03–22.5	0.01	Aydın et al. (2020)
GSPE	ProtG-MBs	1–1 × 10^6	0.3	Tertis et al. (2019b)
Au	CMA	1–15	—	Baraket et al. (2017)
Graphene	AuNP-MWCNT	0.1–1 × 10^3	9 × 10^{-3}	This Work

represent the three consecutive measurements taken for each protein concentration. The coefficient of variance between the redox currents measured by the two systems (CHI 660E vs. the developed potentiostat) was < ±1%.

3.4 Dynamic Response Measurements

The developed potentiostat was also used to measure the dynamic response of the sensor, as shown in **Figure 9A**. The sensor was spiked with increasing IL-10 concentrations ranging from 0.1 pg/ml to 1,000 pg/ml. Four consecutive readings were taken for each concentration in a 6-min timeframe where the sensor response was stable. We determined the sensor's accuracy for analyzing unknown protein concentrations in SWF. The sensor could accurately estimate the concentrations, with a high Pearson correlation coefficient of 0.997, suggesting the excellent reliability of the sensor (**Figure 9B**).

3.5 Reproducibility, Repeatability, and Reversibility Analysis

The reproducibility, repeatability, and reversibility characteristics were analyzed using the CV technique. In order to test for the reproducibility of our device, four identical sensors were tested with the same set of IL-10 levels, and the calibration curves were plotted accordingly (shown in **Figure 10A**). Our sensor indicated an acceptable reproducible behavior with a less than 8% coefficient of variance among the four calibration curves, which is vital for on-body measurements.

Sensor repeatability was tested by repeating the calibration of the same sensor four times in an interval of 1 h. **Figure 10B** demonstrates the four calibration plots obtained with the same sensor. Although the coefficient of variance of the intercept was calculated to be <0.1%, the slope values showed a nearly 10% deviation. This might be due to the continuous exposure of the sensor surface to an uncontrolled humid environment for more than 4 h. Such exposures can be avoided during on-body applications because a medical gauge covers the sensor surface (also explained in the Materials and Methods section). The similar calibration curves demonstrated the repeatable nature of the sensor.

The sensor also demonstrated excellent reversibility, as is illustrated in **Figure 10C**. The sensor was exposed to increasing, followed by decreasing concentrations of IL-10 protein biomarker, and the cycle was repeated four times. The peak oxidation current was almost the same for different cycles with less than 0.1% deviation.

3.6 Drift Analysis

The drift characteristic of the sensor was analyzed using three IL-10 concentrations, including 0.1 pg/ml, 50 pg/ml, and 1,000 pg/ml. The voltammograms were measured every hour over 12 h (**Figure 11A**). The sensor was stored at 4°C between two consecutive test sessions. The overall coefficient of variance was <0.5% indicating the minimal drift displayed by the sensor. The drift behavior was further analyzed in 5 min interval for the same set of IL-10 concentrations over an hour (**Figure 11B**). Again, a minute drift was observed with a coefficient of variance of only 0.001%.

3.7 Selectivity Analysis

To successfully apply the sensor in an actual wound, it is essential to evaluate the sensor response to interfering species present at the wound site. Therefore, the sensor was tested against some common interfering species found at the wound site, such as glucose (180 g/L), cortisol (100 ng/ml), and C-reactive protein (10 pg/ml) (**Figures 12A,B**). The sensor was spiked with three different SWF solutions: 1) a solution containing only interfering species, 2) 10 pg/ml of the target protein (IL-6 or IL-10) mixed with the interfering species, and 3) 500 pg/ml of the target protein (IL-6 or IL-10) mixed with the interfering species. In the absence of target proteins, no current variations were observed with respect to the baseline, while the introduction of target protein (IL-6 or IL-10) generated noticeable current peaks. Further, the effect of interfering species on the sensitivity and response time of the sensors were analyzed (as demonstrated in **Supplementary Figures S5, S6**). It was evident that in the presence of interferents, the sensitivity reduced by <8% and the response was delayed by only 135 s.

3.8 Stability Analysis

To evaluate the long-term stability of the sensor, three sensors were tested for three different IL-10 concentrations over a week. The test results are demonstrated in **Figure 12C**. The sensor was stored at 4°C after each test. The coefficient of variance in the sensor response was measured to be <0.1% over the first 3 days and approximately 5% for the remaining 4 days, indicating an acceptable stable response for on-body measurements under an appropriate storage condition. The stability of the AuNPs-MWCNT coating was further analyzed. The results are reported in the **Supplementary Figure S7**.

4 COMPARISON OF SENSOR PERFORMANCE WITH EXISTING LITERATURE

We further compared the performance of our sensor with some recent electrochemical sensors that are reported in the literature for monitoring IL-6 and IL-10. The comparative analysis is shown in **Table 3**. Our sensor demonstrated a low LoD and wide dynamic range (which covers the IL-6 and IL-10 spectrum after an injury) simultaneously (Kawakami et al., 1997; Pileri et al., 2008), thus depicting an impressive performance compared to recently proposed works.

5 CONCLUSION

In this paper, an IoT-enabled fully integrated and wearable system was developed for multiplexed monitoring of wound biomarkers in real-time. The multiplexed electrochemical sensor featured AuNP decorated MWCNT, which was demonstrated to improve the sensor performance notably. A complete characterization of sensitivity, selectivity, limit of detection, bending, reproducibility, repeatability, reversibility, drift, and stability were performed. Acceptable performance of the sensor in all these test cases demonstrated its future promise for on-body real-time measurements of wound status. Furthermore, our sensor was capable of accurately detecting the protein levels in different pH solutions. Real-time quantification of the inflammation status of the wounds would also enable on-demand drug release at the wound site. Future work involves the integration of a drug delivery mechanism controlled by the real-time protein concentration measured by the sensor. The impact of this work is expected to be tremendous in the field of wound management by providing real-time information on the progression of inflammation at the wound site, thereby allowing the implementation of efficient therapeutic measures. Incorporation of an automated drug delivery mechanism will take this proposed system to the next level of personalized wound care.

DATA AVAILABILITY STATEMENT

The original contributions presented in the study are included in the article/**Supplementary Material**, further inquiries can be directed to the corresponding author.

AUTHOR CONTRIBUTIONS

ST initiated the concept, led the experiments, and supervised the entire project. TN designed and developed the sensor and conducted characterizations and protein tests. NH developed and tested the IoT-enabled potentiostat circuit, performed the bending tests and COMSOL simulation. All the authors contributed to data analysis and manuscript writing.

FUNDING

This project was funded by The University of Texas System Board of Regents' Rising STARs grant.

ACKNOWLEDGMENTS

The authors thank the Shimadzu Institute Nanotechnology Research Center at Arlington, TX, for the SEM imaging facility.

SUPPLEMENTARY MATERIAL

The Supplementary Material for this article can be found online at: https://www.frontiersin.org/articles/10.3389/fnano.2022.851041/full#supplementary-material

REFERENCES

Ali, M. A., Tabassum, S., Wang, Q., Wang, Y., Kumar, R., and Dong, L. (2018). Integrated Dual-Modality Microfluidic Sensor for Biomarker Detection Using Lithographic Plasmonic crystal. *Lab. Chip* 18, 803–817. doi:10.1039/C7LC01211J

Ali, M. A., Hu, C., Jahan, S., Yuan, B., Saleh, M. S., Ju, E., et al. (2020). -J., Panat, RSensing of COVID-19 Antibodies in Seconds via Aerosol Jet Nanoprinted Reduced-Graphene-Oxide-Coated 3D Electrodes. *Adv. Mater.* 33, 7. doi:10.1002/adma.202006647

Ashley, B. K., Brown, M. S., Park, Y., Kuan, S., and Koh, A. (2019). Skin-inspired, Open Mesh Electrochemical Sensors for Lactate and Oxygen Monitoring. *Biosens. Bioelectron.* 132, 343–351. doi:10.1016/j.bios.2019.02.041

Aydın, E. B., Aydın, M., and Sezgintürk, M. K. (2020). The Development of an Ultra-sensitive Electrochemical Immunosensor Using a PPyr-NHS Functionalized Disposable ITO Sheet for the Detection of Interleukin 6 in Real Human Serums. *N. J. Chem.* 44. doi:10.1039/D0NJ03183F

Bandodkar, A. J., Jeerapan, I., and Wang, J. (2016). Wearable Chemical Sensors: Present Challenges and Future Prospects. *ACS. Sens* 1, 5. doi:10.1021/acssensors.6b00250

Baraket, A., Lee, M., Zine, N., Sigaud, M., Bausells, J., and Errachid, A. (2017). A Fully Integrated Electrochemical Biosensor Platform Fabrication Process for Cytokines Detection. *Biosens. Bioelectron.* 93, 170–175. doi:10.1016/j.bios.2016.09.023

Bard, A. J., and Faulkner, L. R. (1980). *Electrochemical Methods: Fundamentals and Applications*. New York, NY, USA: Wiley. ISBN: 978-0-471-04372-0.

Bazbouz, M. B., and Tronci, G. (2019). Two-layer Electrospun System Enabling Wound Exudate Management and Visual Infection Response. *Sensors (Basel)* 19, 5. doi:10.3390/s19050991

Brown, M. S., Ashley, B., and Koh, A. (2018). Wearable Technology for Chronic Wound Monitoring: Current Dressings, Advancements, and Future Prospects. *Front. Bioeng. Biotechnol.* 6, 47. doi:10.3389/fbioe.2018.00047

Clayton, W., and Elasy, T. A. (2009). A Review of the Pathophysiology, Classification, and Treatment of Foot Ulcers in Diabetic Patients. Clin. *Diabetes* 27, 2. doi:10.2337/diaclin.27.2.52

Darby, I. A., Laverdet, B., Bonté, F., and Desmoulière, A. (2014). Fibroblasts and Myofibroblasts in Wound Healing. *Clin. Cosmet. Investig. Dermatol.* 7, 301–311. doi:10.2147/CCID.S50046

Elgrishi, N., Rountree, K. J., McCarthy, B. D., Rountree, E. S., Eisenhart, T. T., and Dempsey, J. L. (2018). A Practical Beginner's Guide to Cyclic Voltammetry. *J. Chem. Educ. No* 95, 2,. doi:10.1021/acs.jchemed.7b00361

Fang, C., Zhang, Y., Zhang, Z., Shan, C., Shen, W., and Jia, X. (2018). Preparation of "Natural" Diamonds by HPHT Annealing of Synthetic Diamonds. *Cryst. Eng. Comm.* 20. doi:10.1039/C7CE02013A

Farahani, M., and Shafiee, A. (2021). Wound Healing: From Passive to Smart Dressings. *Adv. Healthc. Mater.* 10, e2100477–16. doi:10.1002/adhm.202100477

Ghica, M. E., and Brett, C. M. A. (2013). Simple and Efficient Epinephrine Sensor Based on Carbon Nanotube Modified Carbon Film Electrodes. *Anal. Lett.* 46, 9. doi:10.1080/00032719.2012.762584

Gurtner, G. C., Werner, S., Barrandon, Y., and Longaker, M. T. (2008). Wound Repair and Regeneration. *Nature* 453, 314–321. doi:10.1038/nature07039

Han, G., and Ceilley, R. (2017). Chronic Wound Healing: a Review of Current Management and Treatments. *Adv. Ther.* 34, 599–610. 3. doi:10.1007/s12325-017-0478-y

Kassal, P., Zubak, M., Scheipl, G., Mohr, G. J., Steinberg, M. D., and Steinberg, I. M. (2017). Smart Bandage with Wireless Connectivity for Optical Monitoring of pH. *Sens. Actuators B Chem.* 246. doi:10.1016/j.snb.2017.02.095

Kawakami, M., Kaneko, N., Anada, H., Terai, C., and Okada, Y. (1997). *Measurement of Interleukin-6, Interleukin-10, and Tumor Necrosis Factor-Alpha Levels in Tissues and Plasma after thermal Injury in Mice* 121, 4. doi:10.1016/s0039-6060(97)90315-9

Kolaczkowska, E., and Kubes, P. (2013). Neutrophil Recruitment and Function in Health and Inflammation. *Nat. Rev. Immunol.* 13, 159–175. no. 3. doi:10.1038/nri3399

Kundu, S., Tabassum, S., and Kumar, R. (2020). A Perspective on Sepsis Pathogenesis, Biomarkers and Diagnosis: A Concise Survey. *Med. Devices Sensors* 3, 1. doi:10.1002/mds3.10089

Li, S., Renick, P., Senkowsky, J., Nair, A., and Tang, L. (2021). Diagnostics for Wound Infections. *Adv. Wound Care* 10, 6. doi:10.1089/wound.2019.1103

Luo, H., Shi, Z., Li, N., Gu, Z., and Zhuang, Q. (2001). Investigation of the Electrochemical and Electrocatalytic Behavior of Single-wall Carbon Nanotube Film on a Glassy Carbon Electrode. *Anal. Chem.* 73, 915–920. doi:10.1021/ac000967l

Mantovani, A., Biswas, S. K., Galdiero, M. R., Sica, A., and Locati, M. (2013). Macrophage Plasticity and Polarization in Tissue Repair and Remodelling. *J. Pathol.* 229, 176–185. 2. doi:10.1002/path.4133

Mazloum-Ardakani, M., Beitollahi, H., Ganjipour, B., Naeimi, H., and Nejati, M. (2009). Electrochemical and Catalytic Investigations of Dopamine and Uric Acid by Modified Carbon Nanotube Paste Electrode. *Bioelectrochemistry* 75, 1–8. doi:10.1016/j.bioelechem.2008.11.006

McLister, A., Mathur, A., and Davis, J. (2017). Wound Diagnostics: Deploying Electroanalytical Strategies for point of Care Sensors and Smart Dressings. *Curr. Opin. Electrochem.* 3, 1. doi:10.1016/j.coelec.2017.05.002

McLister, A., Phair, J., Cundell, J., and Davis, J. (2014). Electrochemical Approaches to the Development of Smart Bandages: a Mini-Review. *Electrochem. Commun.* 40. doi:10.1016/j.elecom.2014.01.003

Mehmood, N., Hariz, A., Fitridge, R., and Voelcker, N. H. (2014). Applications of Modern Sensors and Wireless Technology in Effective Wound Management. *J. Biomed. Mater. Res. B Appl. Biomater.* 102, 885–895. 4. doi:10.1002/jbm.b.33063

Menke, N. B., Ward, K. R., Witten, T. M., Bonchev, D. G., and Diegelmann, R. F. (2007). Impaired Wound Healing. *Clin. Dermatol.* 25, 19–25. 1. doi:10.1016/j.clindermatol.2006.12.005

Momoh, F. U., Boateng, J. S., Richardson, S. C., Chowdhry, B. Z., and Mitchell, J. C. (2015). Development and Functional Characterization of Alginate Dressing as Potential Protein Delivery System for Wound Healing. *Int. J. Biol. Macromol* 81, 137–150. doi:10.1016/j.ijbiomac.2015.07.037

Mota, F. A. R., Pereira, S. A. P., Araújo, A. R. T. S., Passos, M. L. C., and Saraiva, M. L. M. F. S. (2021). Biomarkers in the Diagnosis of Wounds Infection: an Analytical Perspective. Trends Anal. *Chem.* 143. doi:10.1016/j.trac.2021.116405

Noushin, T., and Tabassum, S. (2022). *WRRIST: A Wearable, Rapid, and Real-Time Infection Screening Tool for Dual-Mode Detection of Inflammatory Biomarkers in Sweat*. San Francisco, CA : SPIE Photonics West [in press].

Novak, M. L., and Koh, T. J. (2013). Macrophage Phenotypes during Tissue Repair. *J. Leukoc. Biol.* 93, 875–881. 6. doi:10.1189/jlb.1012512

O'Callaghan, S., Galvin, P., O'Mahony, C., Moore, Z., and Derwin, R. (2020). 'Smart' Wound Dressings for Advanced Wound Care: a Review. *J. Wound Care* 29, 7. doi:10.12968/jowc.2020.29.7.394

Ochoa, M., Rahimi, R., Zhou, J., Jiang, H., Yoon, C. K., Maddipatla, D., et al. (2020). Integrated Sensing and Delivery of Oxygen for Next-Generation Smart Wound Dressings. *Microsyst. Nanoeng* 6, 46. doi:10.1038/s41378-020-0141-7

Oliveira, S., de, Rosowski, E. E., and Huttenlocher, A. (2016). Neutrophil Migration in Infection and Wound Repair: Going Forward in Reverse. *Nat. Rev. Immunol.* 16. doi:10.1038/nri.2016.49

Oliveira, T. M. B. F., and Morais, S. (2018). New Generation of Electrochemical Sensors Based on Multi-Walled Carbon Nanotubes. *Appl. Sci.* 8, 10. doi:10.3390/app8101925

Pan, N., Qin, J., Feng, P., Li, Z., and Song, B. (2019). Color-changing Smart Fibrous Materials for Naked Eye Real-Time Monitoring of Wound pH. *J. Mater. Chem. B* 7, 2626–2633. doi:10.1039/C9TB00195F

Pereira, A. N., Noushin, T., and Tabassum, S. (2021). "A Wearable, Multiplexed Sensor for Real-Time and *In-Situ* Monitoring of Wound Biomarkers," in *Proc. IEEE Sensors* (Sydney: Australia). doi:10.1109/SENSORS47087.2021.9639722

Pēña, S. G., and O'Neill, L. A. J. (2014). Metabolic Reprogramming in Macrophage Polarization. *Fron. Immunol.* 5. doi:10.3389/fimmu.2014.00420

Phillips, C. J., Humphreys, I., Fletcher, J., Harding, K., Chamberlain, G., and Macey, S. (2016). Estimating the Costs Associated with the Management of Patients with Chronic Wounds Using Linked Routine Data. *Int. Wound J.* 13, 1193–1197. 6. doi:10.1111/iwj.12443

Pileri, D., Accardo Palombo, A., D'Amelio, L., D'Arpa, N., Amato, G., Masellis, A., et al. (2008). Concentrations of Cytokines IL-6 and IL-10 in Plasma of Burn Patients: Their Relationship to Sepsis and Outcome. *Ann. Burns Fire Disasters* 21, 182–185.

Pourshahrestani, S., Zeimaran, E., Kadri, N. A., Mutlu, N., and Boccaccini, A. R. (2020). Polymeric Hydrogel Systems as Emerging Biomaterial Platforms to

Enable Hemostasis and Wound Healing. *Adv. Healthc. Mater.* 9, e2000905. 20. doi:10.1002/adhm.202000905

Sen, C. K., Gordillo, G. M., Roy, S., Kirsner, R., Lambert, L., Hunt, T. K., et al. (2009). Human Skin Wounds: a Major and Snowballing Threat to Public Health and the Economy. *Wound Repair Regen.* 17, 763–771. 6. doi:10.1111/j.1524-475X.2009.00543.x

Serra, M. B., Barroso, W. A., Silva, N., da, N., Selma, do, N. S., Borges, A. C. R., et al. (2017). From Inflammation to Current and Alternative Therapies Involved in Wound Healing. *Int. J. Inflamm.* doi:10.1155/2017/3406215

Shakila, V., and Pandian, K. (2006). Preparation of Gold Nanoislands on Various Functionalized Polymer-Modified Glass and ITO for Electrochemical Characterization of Monolayer Assembly of Alkanethiols. *J. Solid State. Electrochem.* 11. doi:10.1007/s10008-006-0107-1

Silva, W., da, Ghica, M. E., and Brett, C. M. A. (2018). Gold Nanoparticle Decorated Multiwalled Carbon Nanotube Modified Electrodes for the Electrochemical Determination of Theophylline. *Anal. Methods* 10. doi:10.1039/C8AY02150C

Standl, E., Khunti, K., Hansen, T. B., and Schnell, O. (2019). The Global Epidemics of Diabetes in the 21st century: Current Situation and Perspectives. *Eur. J. Prev. Cardiol.* 26, 7–14. doi:10.1177/2047487319881021

Tertis, M., Leva, P. I., Bogdan, D., Suciu, M., Graur, F., and Cristea, C. (2019a). Impedimetric Aptasensor for the Label-free and Selective Detection of Interleukin-6 for Colorectal Cancer Screening. *Biosens. Bioelectron.* 137, 123–132. doi:10.1016/j.bios.2019.05.012

Tertis, M., Ciui, B., Suciu, M., Săndulescu, R., and Cristea, C. (2017). Label-free Electrochemical Aptasensor Based on Gold and Polypyrrole Nanoparticles for Interleukin 6 Detection. *Electrochim. Acta* 258. doi:10.1016/j.electacta.2017.11.176

Tertis, M., Melinte, G., Ciui, B., Simon, I., Stiufiuc, R., Sandulescu, R., et al. (2019b). A Novel Label Free Electrochemical Magnetoimmunosensor for Human Interleukin-6 Quantification in Serum. *Electroanalysis* 31. doi:10.1002/elan.201800620

Thamri, A., Baccar, H., Struzzi, C., Bittencourt, C., Abdelghani, A., and Llobet, E. (2016). MHDA-functionalized Multiwall Carbon Nanotubes for Detecting Non-aromatic VOCs. *Sci. Rep.* 6, 35130. doi:10.1038/srep35130

Tonnesen, M. G., Feng, X., and Clark, R. A. (2000). Angiogenesis in Wound Healing. *J. Investig. Dermatol. Symp. Proc.* 5, 40–46. 1. doi:10.1046/j.1087-0024.2000.00014.x

Turkevich, J., Stevenson, P., and Hillier, J. (1951). A Study of the Nucleation and Growth Processes in the Synthesis of Colloidal Gold. Discuss. *Faraday Soc.* 11, 55–75. doi:10.1039/DF9511100055

Wilgus, T. A., Roy, S., and McDaniel, J. C. (2013). Neutrophils and Wound Repair: Positive Actions and Negative Reactions. *Adv. Wound Care (New Rochelle)* 2, 379–388. doi:10.1089/wound.2012.0383

Williams, J. Z., and Barbul, A. (2003). Nutrition and Wound Healing. *Surg. Clin. North. Am.* 83, 571–596. doi:10.1016/S0039-6109(02)00193-7

Wiorek, A., Parrilla, M., Cuartero, M., and Crespo, G. A. (2020). Epidermal Patch with Glucose Biosensor: pH and Temperature Correction toward More Accurate Sweat Analysis during Sport Practice14. *Anal. Chem.* 92, 10153–10161. doi:10.1021/acs.analchem.0c02211

Wu, K., Wu, X., Chen, M., Wu, H., Jiao, Y., and Zhou, C. (2020). H_2O_2-responsive Smart Dressing for Visible H_2O_2 Monitoring and Accelerating Wound Healing. *Chem. Eng. J.* 387. doi:10.1016/j.cej.2020.124127

Zhou, J., Yao, D., Qian, Z., Hou, S., Li, L., Jenkins, A. T. A., et al. (2018). Bacteria-responsive Intelligent Wound Dressing: Simultaneous *In Situ* Detection and Inhibition of Bacterial Infection for Accelerated Wound Healing. *Biomaterials* 161, 11–23. doi:10.1016/j.biomaterials.2018.01.024

Zi, L., Li, J., Mao, Y., Yang, R., and Qu, L. (2012). High Sensitive Determination of Theophylline Based on Gold Nanoparticles/l-cysteine/Graphene/Nafion Modified Electrode. *Electrochimica Acta* 78. doi:10.1016/j.electacta.2012.06.018

Zimlichman, E., Henderson, D., Tamir, O., Franz, C., Song, P., Yamin, C. K., et al. (2013). Health Care-Associated Infections: a Meta-Analysis of Costs and Financial Impact on the US Health Care System. *JAMA Intern. Med.* 173, 2039–2046. doi:10.1001/jamainternmed.2013.9763

Conflict of Interest: The authors declare that the research was conducted in the absence of any commercial or financial relationships that could be construed as a potential conflict of interest.

Publisher's Note: All claims expressed in this article are solely those of the authors and do not necessarily represent those of their affiliated organizations, or those of the publisher, the editors and the reviewers. Any product that may be evaluated in this article, or claim that may be made by its manufacturer, is not guaranteed or endorsed by the publisher.